

Josephson effect in graphene Corbino disks

Adam Rycerz*

Institute for Theoretical Physics, Jagiellonian University, Łojasiewicza 11, PL–30348 Kraków, Poland

(Dated: March 25, 2026)

Peculiar features of the Josephson effect in graphene were described theoretically by Titov and Beenakker [Phys. Rev. B **74**, 041401(R) (2006)], who solved the Dirac-Bogoliubov-de-Gennes equation for a superconductor-graphene-superconductor junction with rectangular geometry. Here, we adopt the analysis for graphene Corbino disks, finding out that — for the outer to inner radii ratio $r_2/r_1 \gtrsim 5$ — such systems may demonstrate, when varying the electrochemical potential and the spatial profile of the electrostatic barrier, crossover from standard Josephson tunneling (SJT), via graphene-specific multimode Dirac-Josephson tunneling (MDJT), towards the ballistic Josephson effect (BJE). Signatures of SJT appear only near the Dirac point when the barrier shape is close to rectangular, MDJT appears in the tripolar range and is very robust against varying the barrier shape, and BJE is restored in the unipolar range when smoothing the barrier shape. A comparison with the results of a numerical simulation of quantum transport on the honeycomb lattice is also given.

I. INTRODUCTION

The disk-shaped device, consists of an annular conductor, attached to inner and outer highly conducting electrodes covering the inner and outer circular periphery, was considered by Boltzmann in 1886 [1] and by several authors in the early 1900s [2, 3] to measure the magnetoresistance without generating the Hall voltage, making a significant step towards understanding the nature of charge transport in ordinary solids [4]. Later, an interest in — as commonly called — Corbino geometry has reappeared after the fabrication of GaAs/AlGaAs heterostructures [5–8], and the discovery of high-temperature superconductivity [9], as edge-free devices provide valuable insights into the system dynamics.

In the context of graphene, the edge-free Corbino geometry is often considered [10–21], mainly because, in such a geometry, magnetotransport at high fields is unaffected by edge states, allowing one to probe the bulk transport properties [18–21]. Although the Josephson effect in graphene has attracted considerable attention [22–35], the Corbino-Josephson setup (i.e., the disk contacted to superconducting electrodes, see Fig. 1), earlier studied both in superconductor-insulator-superconductor [36] and superconductor-normal metal-superconductor [37] variants, and recently constructed on the surface of topological insulators [38], has been discussed only marginally in the context of graphene [30].

In this paper, we consider the Corbino geometry superconductor-graphene-superconductor junction, focusing on the wide-disk case (the outer radius $r_2 \gg r_1$ —the inner radius). In such a case, in the Dirac point, the transport is governed by two equivalent (and fourfold-degenerate) modes, corresponding to total angular momentum quantum numbers $j = \pm 1/2$, with the transmission probabilities $T_{\pm 1/2} \propto r_1/r_2 \ll 1$ [12, 13]. Therefore, a standard Josephson tunneling (SJT), characterized by a sinusoidal current-phase relation, is expected near the Dirac point, away from which graphene-specific multimode Dirac-Josephson tunnel-

ing (MDJT) [22, 35] may appear. In addition, the radial electrostatic potential profile is tuned, from from a rectangular to a parabolic one, making the device capable of showing also the ballistic Josephson effect (BJE), building analogy with the sub-Sharvin to ballistic crossover predicted for normal metallic electrodes [39, 40].

As our discussion is limited to zero temperature, hydrodynamic effects, which may alter the system characteristics starting from few-kelvin temperatures [41–44], are beyond the scope of this work.

The paper is organized as follows. In Sec. II we present the details of our numerical approach. The results for the Corbino-Josephson setup in graphene with rectangular potential barrier are summarized in Sec. III. The central results of the paper, concerning the critical current and skewness of the current-phase relation for smooth potentials, are presented in

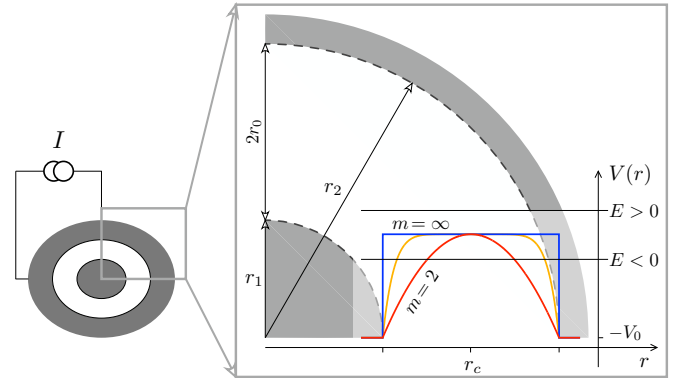


Figure 1: Left: Schematic of a graphene disk with inner radius r_1 and outer radius r_2 , contacted by two circular superconducting electrodes (dark areas). A current source drives a dissipationless supercurrent through the annular region (white). A separate gate electrode (not shown) allows one to tune the carrier concentration around the neutrality point. Right: Electrostatic potential profiles given by Eq. (2) with $m = 2, 8$ and $m = \infty$ (i.e., the rectangular barrier). The Fermi energy E is defined with respect to the top of a barrier. $E > 0$ corresponds to unipolar n-n-n doping in the device; for $E < 0$, circular n-p-n (tripolar) structure is formed. Arcs (dashed lines) mark the interfaces between the disk area [$r_1 < r < r_2$] and contact regions [$r < r_1$ or $r > r_2$].

*Correspondence: rycerz@th.if.uj.edu.pl.

Sec. IV. A comparison with the tight-binding simulation of quantum transport is provided in Sec. V. The concluding remarks are given in Sec. VI.

II. MODEL AND METHODS

A. Dirac Hamiltonian for the normal state

In typical graphene nanosystems, boundary effects may strongly affect transport properties of the system, not only near the Dirac point, where the transport is governed by one (or a few) discrete modes [45, 46] but also away from the Dirac point [47], albeit to a smaller degree. In the case of edge-free Corbino geometry, the role of the boundary effects is eliminated; instead, the role of interfaces separating the sample and the leads becomes essential. In particular, for normal metallic leads, significant particle-hole asymmetry of the conductance spectrum was observed [15, 20, 48]; namely, the conductance for the chemical potential $\mu < 0$ (defined with respect to the charge-neutrality point) is noticeably suppressed compared with the $\mu > 0$ range. This observation is interpreted in terms of additional, contact resistance which is amplified in case of tripolar n-p-n doping, compared to unipolar n-n-n doping, as the the circular p-n junctions introduce additional backscattering of electrons in the former case. In Ref. [39], a simple model capable of providing a qualitatively correct description of the above-mentioned asymmetry, is put forward. (Such a feature is also correctly reproduced by a model assuming the trapezoidal potential barrier [49], which allows a fully analytical treatment; but this approach produces an artificial conductance maximum near $\mu = 0$.)

Our approach starts from the Dirac Hamiltonian for low-energy excitations in graphene in the normal state, for K valley,

$$\mathcal{H}_0 = v_F \mathbf{p} \cdot \boldsymbol{\sigma} + V(\mathbf{r}), \quad (1)$$

with $v_F = \sqrt{3} t_0 a_0 / (2\hbar) \approx 10^6$ m/s the energy-independent Fermi velocity ($t_0 = 2.7$ eV is the nearest-neighbor hopping integral and $a_0 = 0.246$ is the lattice parameter), and $\mathbf{p} = (p_x, p_y)$ the in-plane momentum operator (with $p_j = -i\hbar\partial_j$), $\boldsymbol{\sigma} = (\sigma_x, \sigma_y)$ (with σ_j being the Pauli matrices). For the forthcoming numerical calculations, we set (in the physical units) $\hbar v_F = 0.575214$ eV·nm. The electrostatic potential energy in Eq. (1) depends — in the polar coordinates (r, φ) — only on r , and is given by

$$V(\mathbf{r}) = V(r) = -V_0 \times \begin{cases} 1 & \text{if } |r - r_c| > r_0, \\ \frac{|r - r_c|^m}{r_0^m} & \text{if } |r - r_c| \leq r_0, \end{cases} \quad (2)$$

where we have defined $r_c = (r_1 + r_2)/2$ and $r_0 = (r_2 - r_1)/2$. In particular, the limit of $m \rightarrow \infty$ corresponds to the rectangular barrier (with a cylindrical symmetry); any finite $m \geq 2$ defines a smooth potential barrier, interpolating between the parabolic ($m = 2$) and rectangular ($m = \infty$) shape. In principle, barrier smoothing can be regarded as a feature of a self-consistent solution originating from the diffusion of carriers;

we expect this feature to strongly depend on the experimental details, with graphene-on-hBN devices [18] showing rectangular, rather than smooth, profiles.

B. The Dirac-Bogoliubov-De-Gennes equation

In the presence of superconducting leads (the $r < r_1$ and $r > r_2$ regions) we employ the Dirac-Bogoliubov-de Gennes equation [22, 23]

$$\begin{pmatrix} \mathcal{H}_0 - \mu & \Delta \\ \Delta^* & \mu - \overline{\mathcal{H}}_0 \end{pmatrix} \begin{pmatrix} \Psi_e \\ \Psi_h \end{pmatrix} = \varepsilon \begin{pmatrix} \Psi_e \\ \Psi_h \end{pmatrix}. \quad (3)$$

Here, Ψ_e and Ψ_h are the electron and hole wave functions, $\varepsilon > 0$ is the excitation energy, and $\mu = E$ — the Fermi energy — since the $T = 0$ case is considered. In the absence of a magnetic field, the Hamiltonian is time-reversal invariant, $\overline{\mathcal{H}}_0 = \mathcal{T}\mathcal{H}_0\mathcal{T}^{-1} = \mathcal{H}_0$, with \mathcal{T} the time-reversal operator [50].

The complex pair potential Δ in Eq. (3) depends only the radial coordinate (r), and is truncated by adopting the step-function model for the two interfaces between the normal region and superconductors at $r = r_1$ and $x = r_2$, namely

$$\Delta(\mathbf{r}) = \Delta(r) = \begin{cases} \Delta_0 e^{i\theta/2} & \text{if } r < r_1, \\ 0 & \text{if } r_1 \leq r \leq r_2, \\ \Delta_0 e^{-i\theta/2} & \text{if } r > r_2, \end{cases} \quad (4)$$

with the bulk superconducting gap Δ_0 and the phase difference between the superconductors θ .

As shown in Refs. [22, 23], by analyzing the spectrum of Andreev states for $\varepsilon < \Delta_0$ for the short-junction limit, i.e., $r_2 - r_1 \ll \xi_0$ (with the superconducting coherence length $\xi_0 = \hbar v_F / \Delta_0$; for instance, $\xi_0 \approx 550$ nm for superconducting electrodes made with molybdenum rhenium [28]), the Josephson current can be written as

$$I(\theta) = \frac{e\Delta_0}{\hbar} \sum_j \frac{T_j \sin \theta}{\sqrt{1 - T_j \sin^2(\theta/2)}}, \quad (5)$$

while the normal-state resistance is given by

$$R_N^{-1} = \frac{4e^2}{\hbar} \sum_j T_j. \quad (6)$$

In effect, both quantities are determined by the transmission probabilities T_j characterizing a graphene sample between two electrodes in the normal state ($\Delta_0 = 0$). Eqs. (5) and (6) coincide, respectively, with the multichannel mesoscopic Josephson equation [51] and the Landauer-Büttiker formula [52]; both formulas are multiplied by a factor of two due to the additional (valley) degeneracy in graphene.

C. Mode-matching method

For the Corbino geometry, the transmission probabilities in Eqs. (5) and (6), each of which is attributed to the j -th normal mode, with the total angular momentum quantum number

$j = \pm 1/2, \pm 3/2, \dots$, can be found by solving the scattering problem for the Dirac equation, $\mathcal{H}_0 \Psi = E \Psi$. Because of the symmetry of the problem, we can search for the wave function in the form

$$\Psi_j(r, \varphi) = e^{i(j-1/2)\varphi} \begin{pmatrix} \chi_a \\ \chi_b e^{i\varphi} \end{pmatrix}, \quad (7)$$

with the components $\chi_a = \chi_a(r)$, $\chi_b = \chi_b(r)$. Substituting the above into the Dirac equation immediately brings us to the system of ordinary differential equations

$$\chi'_a = \frac{j-1/2}{r} \chi_a + i \frac{E-V(r)}{\hbar v_F} \chi_b, \quad (8)$$

$$\chi'_b = i \frac{E-V(r)}{\hbar v_F} \chi_a - \frac{j+1/2}{r} \chi_b, \quad (9)$$

where primes denote derivatives with respect to r .

For the leads, $r < r_1$ or $r > r_2$, the electrostatic potential energy is constant, $V(r) = -V_0$. Assuming $E > -V_0$ (electron doping), we can find the solutions $\chi_j = (\chi_{j,a}, \chi_{j,b})^T$ analytically,

$$\chi_j^{(+)} = \begin{pmatrix} H_{j-1/2}^{(2)}(Kr) \\ iH_{j+1/2}^{(2)}(Kr) \end{pmatrix}, \quad \chi_j^{(-)} = \begin{pmatrix} H_{j-1/2}^{(1)}(Kr) \\ iH_{j+1/2}^{(1)}(Kr) \end{pmatrix}, \quad (10)$$

where the upper index (\pm) marks the incoming (i.e., propagating from $r = 0$) or the outgoing (propagating from $r = \infty$) wave, $H_\nu^{(1)}(\rho)$ [$H_\nu^{(2)}(\rho)$] is the Hankel function of the first [second] kind, and $K = |E + V_0|/(\hbar v_F)$. Using the above as a basis set, we write down full wavefunctions (corresponding to a given j) for the two leads,

$$\chi_j^{(\text{inner})} = \chi_j^{(+)} + r_j \chi_j^{(-)}, \quad r < r_1, \quad (11)$$

$$\chi_j^{(\text{outer})} = t_j \chi_j^{(+)}, \quad r > r_2, \quad (12)$$

where we have introduced the reflection (r_j) and transmission coefficient (t_j).

For the disk area, $r_1 < r < r_2$, Eqs. (8), (9) typically need to be integrated numerically. The details of the calculations will be given later; it is now sufficient impose the boundary conditions $\chi_j^{(A,B)} \Big|_{r=r_1} = (1, \pm 1)^T$ for the two linearly-independent solutions, allowing us to write down

$$\chi_j^{(\text{disk})} = A_j \chi_j^{(A)} + B_j \chi_j^{(B)}, \quad (13)$$

where A_j, B_j , are arbitrary complex coefficients.

The matching conditions for $r = r_1$ and $r = r_2$ bring us to the linear system of equations for A, B, r_j , and t_j ,

$$\begin{bmatrix} \chi_{j,a}^{(-)}(r_1) & -\chi_{j,a}^{(A)}(r_1) & -\chi_{j,a}^{(B)}(r_1) & 0 \\ \chi_{j,b}^{(-)}(r_1) & -\chi_{j,b}^{(A)}(r_1) & -\chi_{j,b}^{(B)}(r_1) & 0 \\ 0 & -\chi_{j,a}^{(A)}(r_2) & -\chi_{j,a}^{(B)}(r_2) & \chi_{j,a}^{(+)}(r_2) \\ 0 & -\chi_{j,b}^{(A)}(r_2) & -\chi_{j,b}^{(B)}(r_2) & \chi_{j,b}^{(+)}(r_2) \end{bmatrix} \begin{bmatrix} r_j \\ A_j \\ B_j \\ t_j \end{bmatrix} = \begin{bmatrix} -\chi_{j,a}^{(+)}(r_1) \\ -\chi_{j,b}^{(+)}(r_1) \\ 0 \\ 0 \end{bmatrix}, \quad (14)$$

where we have explicitly written the spinor components of relevant wavefunctions appearing on the right-hand sides of Eqs. (11), (12), and (13).

Solving Eq. (14), one finds the transmission amplitude t_j for a given j and $E = \mu$, and the corresponding transmission probability $T_j(\mu) = |t_j|^2$. The supercurrent $I(\theta)$ and the normal-state resistance R_N are then determined from Eqs. (5) and (6) by summing over the modes.

III. RECTANGULAR POTENTIAL BARRIER

A. Analytic solution

For a rectangular barrier of infinite height, corresponding to $m \rightarrow \infty$ and $V_0 \rightarrow \infty$ in Eq. (2), solutions for the leads ($r < r_1$ or $r > r_2$), see Eq. (10), are replaced with asymptotic

forms,

$$\chi^{(+)} \simeq \frac{e^{iKr}}{\sqrt{r}} \begin{pmatrix} 1 \\ 1 \end{pmatrix}, \quad \chi^{(-)} \simeq \frac{e^{-iKr}}{\sqrt{r}} \begin{pmatrix} 1 \\ -1 \end{pmatrix}. \quad (15)$$

Solution for the disk ($r_1 < r < r_2$) can be written as [12]

$$\chi_j^{(\text{disk})} = A_j \begin{pmatrix} H_{j-1/2}^{(2)}(kr) \\ i\eta H_{j+1/2}^{(2)}(kr) \end{pmatrix} + B_j \begin{pmatrix} H_{j-1/2}^{(1)}(kr) \\ i\eta H_{j+1/2}^{(1)}(kr) \end{pmatrix}, \quad (16)$$

where $k = |E|/(\hbar v_F)$, the doping sign $\eta = \text{sgn } E = \pm 1$ (with $\eta = +1$ indicating electron doping and $\eta = -1$ indicating hole doping).

In turn, solving Eq. (14) leads to [53]

$$T_j = |t_j|^2 = \frac{16}{\pi^2 k^2 r_1 r_2} \frac{1}{\left[\mathfrak{D}_j^{(+)} \right]^2 + \left[\mathfrak{D}_j^{(-)} \right]^2}, \quad (17)$$

Table I: The normal-state conductance R_N^{-1} , the product of critical current I_c and R_N , and the skewness of the current-phase relation S for the Corbino-Josephson setup in graphene in the high-doping limit ($|\mu| \gg \hbar v_F/r_1$), and at the Dirac point ($\mu = 0$), for different values of the disk radii ratio r_2/r_1 . The Sharvin and pseudodiffusive conductance is given by $G_{\text{Sharvin}} = 2g_0 j_{\text{max}}$, with $g_0 = 4e^2/h$ and $j_{\text{max}} = r_1|\mu|/(\hbar v_F)$, and $G_{\text{diff}} = 2g_0/\ln(r_2/r_1)$ (respectively). The analytic (or asymptotic) results are given if available.

r_2/r_1	$ \mu \gg \hbar v_F/r_1$			$\mu = 0$		
	$R_N^{-1}/G_{\text{Sharvin}}$	$I_c R_N e/\Delta_0$	S	R_N^{-1}/G_{diff}	$I_c R_N e/\Delta_0$	S
1	$\pi/4$	2.42851	0.416008	1	2.08207	0.254796
1.1	0.806375	2.43099	0.415441	1.00000	2.08207	0.254796
1.25	0.821914	2.43436	0.414544	1.00000	2.08207	0.254796
2	0.846108	2.44141	0.412430	0.999963	2.07168	0.240120
5	0.856558	2.44504	0.411246	0.946965	1.86653	0.122364
10	0.857949	2.44554	0.411080	0.770470	1.72591	0.063076
∞	$4-\pi$	2.44571	0.411023	$\simeq 4 \ln x/x^a$	$\pi/2$	0

^{a)} Asymptotic behavior, $x = r_2/r_1$.

where

$$\mathfrak{D}_j^{(\pm)} = \text{Im} \left[H_{j-1/2}^{(1)}(kr_1) H_{j\pm 1/2}^{(2)}(kr_2) \pm H_{j+1/2}^{(1)}(kr_1) H_{j\pm 1/2}^{(2)}(kr_2) \right]. \quad (18)$$

Probably, the most surprising feature of the above result is that taking the limit of $U_0 \rightarrow \infty$ does not give $T_j \rightarrow 0$ for all j -s; instead, there is a set of $T_j \sim 1$ for $|j| \lesssim kR_i$. (The corresponding discussion for the Corbino disk in 2DEG can be found in Ref. [12].)

B. The Dirac point

In the limit of $k \rightarrow 0$, Eqs. (17), (18) simplify to

$$T_j(0) = \frac{1}{\cosh^2[j \ln(r_2/r_1)]} = \frac{4}{(r_2/r_1)^j + (r_1/r_2)^j}. \quad (19)$$

For $r_2/r_1 \rightarrow 1$ (the narrow-disk limit), one can approximate the summations in Eqs. (5) and (6) by integrations over continuous $-\infty < j < \infty$, reproducing the results reported in Refs. [22, 23] for the Dirac point ($\mu = 0$)

$$I(\theta) = \frac{e\Delta_0}{\hbar} \frac{4}{\ln(r_2/r_1)} \cos(\theta/2) \text{artanh}[\sin(\theta/2)], \quad (20)$$

and

$$R_N^{-1} = \frac{8e^2}{\hbar} \frac{1}{\ln(r_2/r_1)} \equiv G_{\text{diff}}, \quad (21)$$

with the sample aspect ratio W/L replaced by $2\pi/\ln(r_2/r_1)$. Finding the maximum of $I(\theta)$ at $\theta = \theta_c$ numerically, we get

$$I_c R_N \frac{e}{\Delta_0} = 2.08207 \quad \text{and} \quad S = 0.254796, \quad (22)$$

with the skewness of the current-phase relation $S = 2\theta_c/\pi - 1$. We further notice that the normal-state conductance

(G_{diff}) given in Eq. (21) corresponds to the case of diffusive disk characterized by the universal conductivity of $\sigma_0 = (4/\pi) e^2/h$.

For the wide-disk limit $r_2 \gg r_1$ and for $\mu = 0$, the quantities given by Eqs. (5) and (6) are governed by two equivalent modes with $j = \pm 1/2$, for which $T_j \simeq 4r_1/r_2 \ll 1$. Subsequently, Eq. (5) can be linearized in T_j , with the result

$$I(\theta) \simeq \frac{e\Delta_0}{2\hbar} \sum_{j=\pm 1/2} T_j \sin \theta = \frac{\pi\Delta_0}{2e} R_N^{-1} \sin \theta, \quad (23)$$

giving the characteristics of standard Josephson tunneling (SJT) [51], i.e.,

$$I_c R_N \frac{e}{\Delta_0} = \frac{\pi}{2} \quad \text{and} \quad S = 0. \quad (24)$$

C. The high-doping limit

For the high-doping limit ($|\mu| \gg \hbar v_F/r_1$), we adopt here the approximation technique presented in Ref. [40]. In brief, it is sufficient to restrict the discussion to $-j_{\text{max}} \leq j \leq j_{\text{max}}$, with $j_{\text{max}} = r_1|\mu|/(\hbar v_F)$, and to replace the sums in Eqs. (5) and (6) with integrals over j . What is more, due to the presence of two collinear interfaces separating the sample and the leads, first at $r = r_1$ and second at $r = r_2$, the transmission probability T_j can be approximated using the double-contact formula [54],

$$T_j \simeq T_{j,\phi} = \frac{T_1 T_2}{1 + R_1 R_2 - 2\sqrt{R_1 R_2} \cos \phi}, \quad (25)$$

where the transmission and reflection on the two interfaces read

$$T_1(j) = \frac{2\sqrt{1 - (j/j_{\text{max}})^2}}{1 + \sqrt{1 - (j/j_{\text{max}})^2}}, \quad (26)$$

$$T_2(j) = T_1(jr_1/r_2), \quad (27)$$

$$R_l(j) = 1 - T_l(j), \quad l = 1, 2, \quad (28)$$

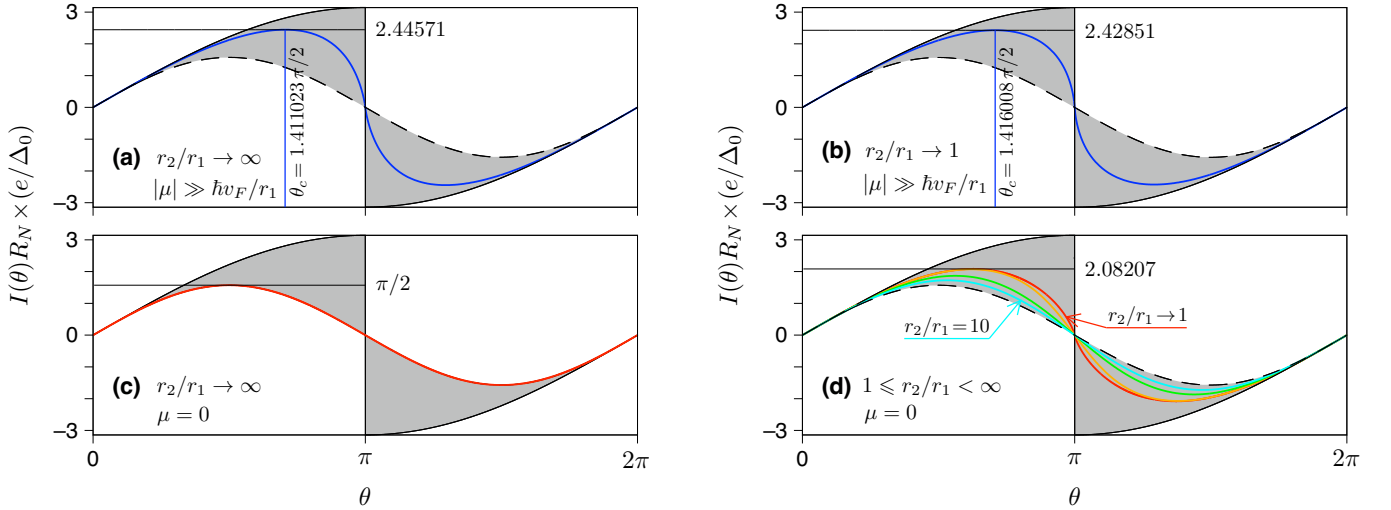


Figure 2: (a)–(d) Current-phase relation for the Corbino-Josephson setup in graphene in the case of rectangular potential barrier and infinitely-doped leads, corresponding to $m \rightarrow \infty$ and $V_0 \rightarrow \infty$ in Eq. (2). (a,b) The high-doping limit ($|\mu| \gg \hbar v_F/r_1$), (c,d) the Dirac point ($\mu = 0$). The radii ratio r_2/r_1 is specified at each panel. Results obtained from Eq. (29) are displayed with blue thick lines in (a,b); red thick line visualizes Eq. (23) in (c) or Eq. (20) in (d). Remaining color thick lines in (d) visualize Eq. (5) with the probabilities $T_j(0)$ given by Eq. (19) calculated for $r_2/r_1 = 2$ (orange), $r_2/r_1 = 5$ (green), and $r_2/r_1 = 10$ (cyan). Thin black lines in all panels visualize the tunneling limit, see Eq. (23) (dashed lines), and the ballistic limit, see Eq. (34) (solid lines).

and ϕ is a phase gained between the scattering events, later assumed to be a random. In turn,

$$I(\theta) \simeq \frac{e\Delta_0}{\hbar} \int_{-j_{\max}}^{j_{\max}} dj \frac{1}{2\pi} \int_{-\pi}^{\pi} d\phi \frac{T_{j,\phi} \sin \theta}{\sqrt{1 - T_{j,\phi} \sin^2(\theta/2)}}, \quad (29)$$

where the last integration represents the averaging over a random ϕ . For the normal-state resistance, the analogous integrations can be performed analytically, leading to

$$R_N^{-1} = 2g_0 \int_0^{j_{\max}} dj \frac{1}{2\pi} \int_{-\pi}^{\pi} d\phi T_{j,\phi} = G_{\text{Sharvin}} \frac{(2c + \frac{1}{c}) \arcsin c + 3\sqrt{1 - c^2} - \frac{\pi}{2}(c^2 + 2)}{1 - c^2}, \quad (30)$$

where we have defined $g_0 = 4e^2/h$ (the conductance quantum for graphene), used parity of Eq. (25) upon $j \leftrightarrow -j$ and $\phi \leftrightarrow -\phi$ to shrink the integration ranges, introduced $G_{\text{Sharvin}} = 2g_0 j_{\max}$ being the Sharvin conductance for a disk, and defined the inverse radii ratio $c = r_1/r_2 < 1$.

In particular, for the narrow-disk limit ($r_2/r_1 \rightarrow 1$), the two interfaces become equivalent ($T_1 = T_2$ and $R_1 = R_2$), and the numerical optimization for Eq. (29), with respect to θ , reproduces the results presented in Ref. [35],

$$I_c R_N \frac{e}{\Delta_0} \simeq 2.42851 \quad \text{and} \quad S = 0.416008, \quad (31)$$

with $R_N^{-1} = (\pi/4) G_{\text{Sharvin}}$.

In the opposite, wide disk limit ($r_2 \gg r_1$), transmission via the second interface becomes perfect ($T_2 = 1$, $R_2 = 0$), and the value of $T_{j,\phi}$ given by Eq. (25) is ϕ -independent, leading

to the result of

$$I_c R_N \frac{e}{\Delta_0} \simeq 2.44571 \quad \text{and} \quad S = 0.411023, \quad (32)$$

with $R_N^{-1} = (4 - \pi) G_{\text{Sharvin}}$.

It must be noticed that the dimensionless characteristics given in Eqs. (31) and (32) are very close to each other; together with the so-called *pseudodiffusive* values given in Eq. (22), they define the borders of graphene-specific multimode Dirac-Josephson tunneling (MDJT) on the $(I_c R_N, S)$ diagram discussed later in this paper.

In Table I, we list the values of $I_c R_N$ and S for six finite values of $r_2/r_1 = 1.1 \div 10$, both for the high-doping limit ($|\mu| \gg \hbar v_F/r_1$) and for the Dirac point ($\mu = 0$), together with the limiting results for $r_2/r_1 \rightarrow 1$ and $r_2/r_1 \rightarrow \infty$ presented above.

The corresponding current-phase relations $I(\theta)$, obtained numerically from Eqs. (20), (23) and (29), are displayed in

Figs. 2(a)–(c). Remarkably, the results for the Dirac point ($\mu = 0$) and finite r_2/r_1 , see Fig. 2(d) [solid lines], obtained by the numerical summation over j -s in Eqs. (5) and (6) with $T_j(0)$ given by Eq. (19), demonstrate gradual evolution — with increasing r_2/r_1 — between the limiting curves for $r_2/r_1 \rightarrow 1$ (red solid line) and for the SJT limit, $r_2/r_1 \rightarrow \infty$ [black dashed line]. (Notice that only the lines for $r_2/r_1 = 2, 5,$ and 10 are displayed, since for $r_2/r_1 \leq 1.25$ the overlap with the $r_2/r_1 \rightarrow 1$ results are almost perfect.)

Also in Figs. 2(a)–(d), we display [with thin solid lines] the current-phase relation for a perfect ballistic system (or Sharvin contact). For such a system, transmission eigenvalues are equal to either 0 or 1, and can be ordered such that

$$T_n = \begin{cases} 1, & 0 \leq n < N_0, \\ 0, & N_0 \leq n < N, \end{cases} \quad (33)$$

with the number of open channels $N_0 \ll N$. Substituting the above to Eqs. (5) and (6) brings us to

$$I(\theta) = N_0 \frac{e\Delta_0}{\hbar} \sin(\theta/2) \operatorname{sgn}(\cos \theta/2), \quad (34)$$

where $\operatorname{sgn}(x)$ is the sign function, and

$$R_N^{-1} = N_0 \frac{4e^2}{h}. \quad (35)$$

In effect, for the ballistic Josephson effect (BJE)

$$I_c R_N \frac{e}{\Delta_0} = \pi \quad \text{and} \quad S = 1. \quad (36)$$

D. The critical current—skewness diagram

In Fig. 3, we present the product $I_c R_N$ as a function of skewness S , using the data of Table I. Hereinafter, the pairs of $(I_c R_N, S)$ defined by Eqs. (22) and (31), are chosen as bounds the MDJT range (indicated with a double arrow).

In order to rationalize our numerical results for the Corbino-Josephson setup in graphene, we consider (as a first toy-model) the case of a single nonzero eigenvalue, $0 < T \leq 1$ in Eqs. (5) and (6). Straightforward optimization of $I(\theta)$ with respect to θ leads to the dependence of $I_c R_N$ versus S presented with a black solid line in Fig. 3. The characteristics of such a *single-mode Josephson junction* are quite distant from the results for the Corbino-Josephson setup, except from the data for $\mu = 0$ and $r_2/r_1 \gtrsim 5$, where the system enters the SJT range.

To construct an alternative *multimode toy model* that parametrizes the tunneling-to-ballistic crossover, we propose the following transmission-angular momentum dependence

$$T_j^{(\Theta)} = \frac{1}{e^{j-\Theta} + 1} - \frac{1}{e^{j+\Theta} + 1} \quad (\Theta > 0). \quad (37)$$

It is also supposed that $j_{\max} \gg 1$, and thus the summations in Eqs. (5) and (6) are replaced by integrations over $-\infty <$

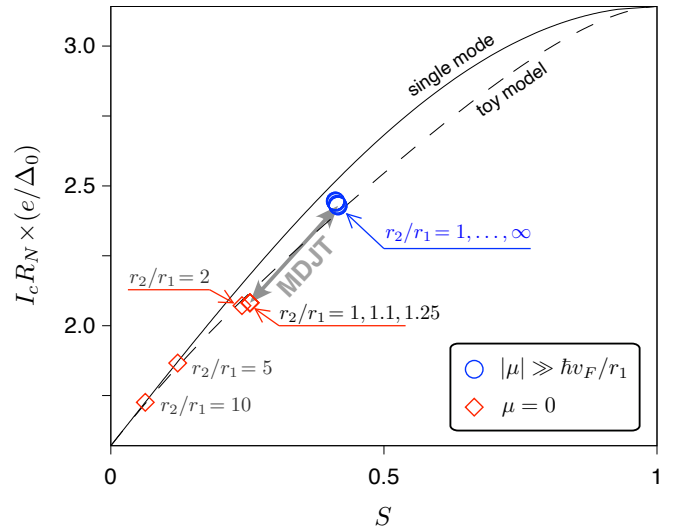


Figure 3: Product of critical current and normal-state resistance $I_c R_N$ displayed versus skewness of the current-phase relation (datapoints). Two datasets represent the results of Table I, for the high-doping limit ($|\mu| \gg \hbar v_F / r_1$) [circles], and for the Dirac point ($\mu = 0$) [diamonds]. Double arrow indicates the multimode Dirac-Josephson tunneling (MDJT) regime, bounded by the $(I_c R_N, S)$ values given in Eqs. (22) and (31). Black solid line presents the results following from the optimization of Eq. (5) for a single nonzero eigenvalue $0 < T \leq 1$; black dashed line depicts the results obtained within the multimode toy model defined by Eq. (37).

$j < \infty$. For instance, $\Theta \rightarrow 0$ reproduces the tunneling limit, with the values of $I_c R_N$ and S given by Eq. (24), whereas $\Theta \gg 1$ corresponds to the ballistic limit. (To be more specific, the value of $I_c R_N$ given in Eq. (36) is reproduced with an accuracy better than 1% for $\Theta \geq 1200$; the same applies for S , starting from $\Theta = 4 \cdot 10^4$.)

The functional dependence of $I_c R_N$ on S , which follows from Eq. (37), is also visualized in Fig. 3 (dashed line). We find that such dependence can be approximated by

$$I_c R_N \frac{e}{\Delta_0} \simeq \frac{\pi}{2} (S + 1) + 0.59 S^{0.89} (1 - S)^{0.70}. \quad (38)$$

The corresponding curve is omitted since it matches the dotted line in Fig. 3 perfectly.

As the current-phase relation for $r_2/r_1 = 5$, see Fig. 2(d) [green solid line], as well as the corresponding $(I_c R_N, S)$ points in Fig. 3, lay relatively far from both the $r_2/r_1 \rightarrow 1$ and $r_2/r_1 \rightarrow \infty$ limits, this value is selected for the numerical analysis of smooth potentials presented in next Section.

IV. SMOOTH POTENTIALS

A. The system and computation details

So far, we have focused on the limits of $|\mu| \gg \hbar v_F / r_1$ and $\mu \ll \hbar v_F / r_1$, for which several analytic results are available. Now, we look at the finite range of $|\mu| \leq 0.4$ eV, comparable with the range accessible for graphene-on-hBN devices

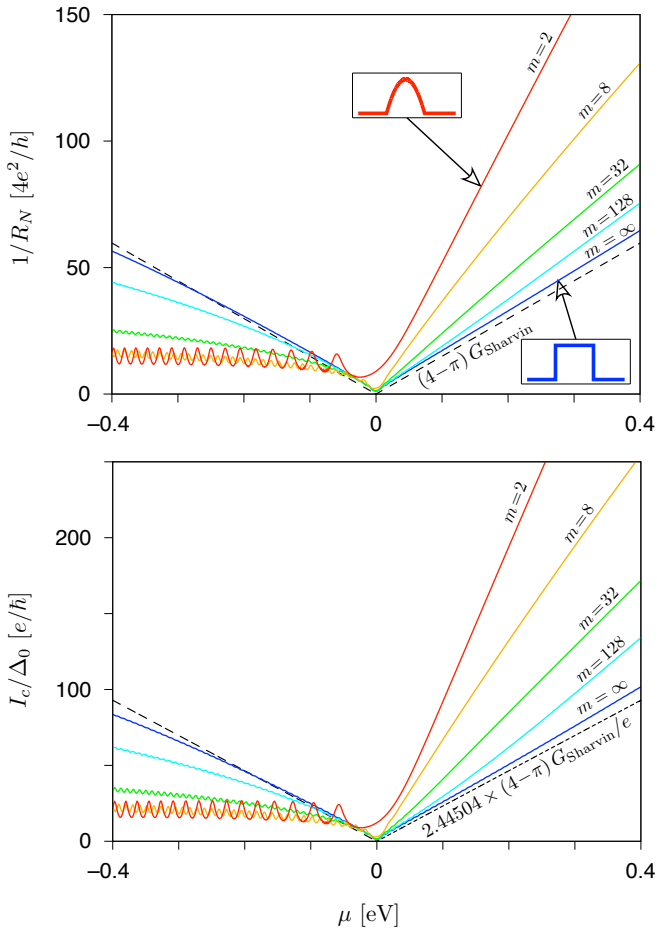


Figure 4: Normal-state conductance $1/R_N$ (top) and critical current I_c (bottom) for the system of Fig. 1 as functions of the chemical potential ($\mu = E$). The parameters are: $r_2 = 5r_1 = 250$ nm, $V_0 = t_0/2 = 1.35$ eV. The exponent m in Eq. (2) is specified for each dataset (solid lines). Insets (top) depict the potential profiles for $m = 2$ and $m = \infty$. Dashed line depicts the sub-Sharvin conductance and the corresponding critical current for $r_2/r_1 \rightarrow \infty$, see Eq. (32).

[18]. As the essential transport characteristics for Corbino disks in graphene saturate (i.e., become very close to their limiting values for $r_2/r_1 \rightarrow 1$) for $r_2/r_1 \lesssim 2$ [13, 40], we take a wider disk, with the radii at $r_2 = 5r_1 = 250$ nm, allowing one to expect the intermediate features between the SJT and MDJT regimes (see Sec. III). Such choice also defines the energy scale that separates the weak- and the high-doping regimes at $\hbar v_F/r_1 = 11.5$ meV. The step height in Eq. (2) is $V_0 = t_0/2 = 1.35$ eV, which yields (for instance) the number of propagating modes in the inner lead as 216 for $\mu = -0.1$ eV and 252 for $\mu = 0.1$ eV.

The numerical integration of Eqs. (8) and (9) was performed utilizing a standard fourth-order Runge-Kutta (RK4) algorithm, with a spatial step of $\Delta x = L/80000 = 2.5$ pm. (For each value of j , the wavefunctions analogous to those given in Eqs. (11) and (12), but describing scattering from $r = \infty$ towards $r = 0$, were used to construct the linear system analogous to Eq. (14), which was then solved to find the

amplitudes t'_j and r'_j , and to check the unitarity of the scattering matrix \mathcal{S} ; the above parameters result in an unitarity error $\epsilon_n = \|\mathcal{S}\mathcal{S}^\dagger - I\| \lesssim 10^{-5}$, with $\|M\|$ denoting the maximum absolute value of a matrix element M_{ij} and the identity matrix I , for all cases considered.) Summation over the modes in Eqs. (5), (6) was terminated if $T_n < 10^{-6}$.

B. Transport characteristics

The evolution of the conductance spectrum with exponent m in Eq. (2), which was discussed earlier in Ref. [40], but only for $r_2/r_1 \leq 2$, is visualized in the top panel of Fig. 4. The bottom panel of Fig. 4 presents a similar evolution of the critical current. Remarkably, the behavior of the two physical properties is very similar, particularly in the tripolar regime ($\mu < 0$). For the unipolar regime ($\mu > 0$), I_c decays slightly slower than $1/R_N$ with the increasing m , particularly for smaller m -s.

A deeper insight into the system behavior is provided by the evolution of the product $I_c R_N$ and the skewness S , as shown in Fig. 5. It is noticeable that the numerical results for smooth potentials and finite V_0 stay in the graphene-specific MDJT range, which is defined by the values obtained for $r_2/r_1 \rightarrow 1$ for the rectangular barrier of an infinite height for $\mu = 0$ and $|\mu| \gg \hbar v_F/r_1$, see Eqs. (22) and (31), provided that the system is in the tripolar regime ($\mu < 0$). In contrast, in the unipolar regime ($\mu > 0$), $I_c R_N$ evolves — with the increasing m — from the values close to the ballistic limit, see Eq. (36), towards graphene-specific values.

In the vicinity of the Dirac point, $|\mu| \ll \hbar v_F/r_1$, the tunneling limit, see Eq. (24), is approached for high m -s; the graphene-specific range is re-entered for lower m -s. Such a feature is virtually invisible for both $1/R_N$ and I_c , see Fig. 4 suggesting that intensive quantities, such as the product $I_c R_N$ and the skewness S , are better probes of graphene-specific features in superconductor-graphene-superconductor systems. We also notice here that the existing experimental measurements of S for rectangular Josephson junctions in graphene seem to be weakly affected by contact resistances, for instance Refs. [27, 28] report values of $S \approx 0.2 \div 0.25$ near the Dirac point, as well as in the tripolar regime.

For a somewhat more detailed view of the data, we present in Fig. 6 the product $I_c R_N$ as a function of skewness S for five selected values of $\mu = 0, \pm 0.1$ eV, ± 0.2 eV, and ten different values of m ($m = 2, 4, \dots, 512$, and ∞) for each μ . The two $(I_c R_N, S)$ pairs, defined by Eqs. (22), (31), and bounding the MDJT regime, are also marked (and indicated with arrows). Additionally, the single-mode approximation, and the results obtained within the multimode toy model, see Eqs. (37) and (38), are visualized in Fig. 6 with solid and dashed lines (respectively).

The values of $(I_c R_N, S)$ for smooth potentials are generally quite distant from the characteristics of a single-mode Josephson junction (see Fig. 6); instead, they are much closer to the results following from the multimode toy model. This feature is particularly striking within (and close to) the MDJT regime (in particular, the values given in Eqs. (22) and (31)

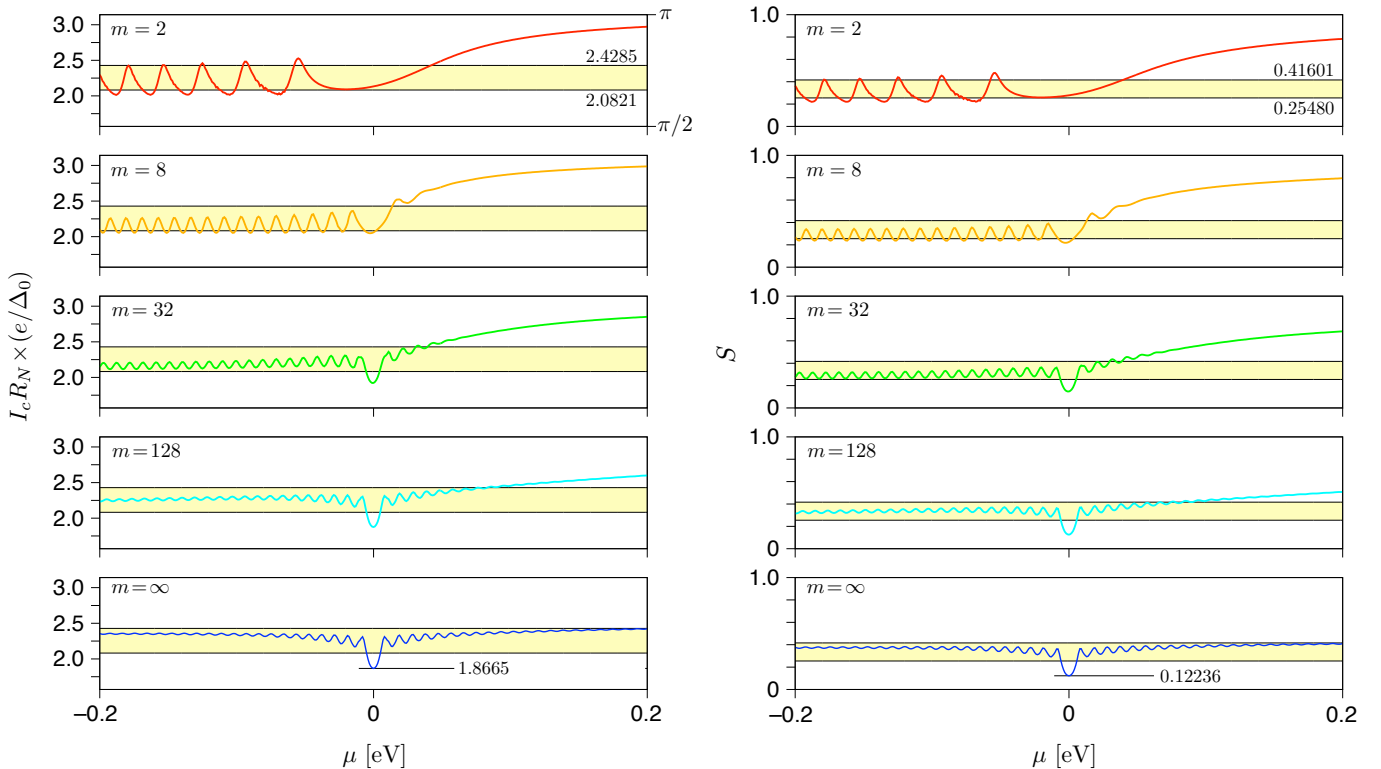


Figure 5: Left: Product $I_c R_N$ for the data shown in Fig. 4. Right: Skewness of the current-phase relation S as a function of the chemical potential for the same system parameters. The exponent m in Eq. (2) is varied between the rows. Horizontal lines bordering the yellow areas mark the MDJT range, defined by the values for rectangular barrier of an infinite height ($m \rightarrow \infty$, $V_0 \rightarrow \infty$), corresponding to $\mu = 0$ and $|\mu| \gg \hbar v_F / r_1$ for the narrow-disk limit, $r_2 / r_1 \rightarrow 1$, see Eqs. (22) and (31); the values for $r_2 / r_1 = 5$ are also marked in the bottom rows.

are well-reproduced for $\Theta \approx 3.4$ and $\Theta \approx 6.8$), but also in the BJE limit. For $\mu = 0$ and large m , where SJT is restored, the single-mode model provides a reasonable approximation for the numerical results.

V. TIGHT-BINDING SIMULATION

For the sake of completeness, we present now the results of tight-binding simulations for the half-Corbino disk — the system earlier studied in Ref. [47]. Going beyond the Dirac equation, the tight-binding model grasps several features of more accurate models, such as the trigonal warping of the dispersion relation, the presence of the van Hove singularity in the density of states, and the short-wavelength cutoff due to the lattice discretization, manifesting itself via limited number of modes in the leads.

A. The Hamiltonian

Although the Hamiltonians with more distant hopping elements were recently discussed [55], here we will limit ourselves to the familiar single-hopping tight binding Hamilto-

nian given by

$$H = \sum_{i,j,s} t_{ij} c_{i,s}^\dagger c_{j,s} + \sum_{i,s} V_i n_{is}, \quad (39)$$

where the indices i, j run over sites in the honeycomb lattice of carbon atoms, and $s = \uparrow, \downarrow$ is the spin up/down orientation. The hopping-matrix elements $t_{ij} = -t_0$ (with $t_0 = 2.7$ eV) if i, j are nearest neighbors; otherwise, $t_{ij} = 0$. For the system depicted in Fig. 7(d), the electrostatic potential energy $V_j = V(\mathbf{r}_j)$ varies according to Eq. (2) in the sample area, and is equal to $-V_0$, with $V_0 = t_0/2 = 1.35$ eV, in the leads. Since the Hamiltonian given by Eq. (39) includes nearest-neighbor hopping elements only, a small deviation of the potential energy, $\delta V_j = 0.01 t_0$, is added for outermost edge atoms in the sample area in order to ensure the physical character of the current density distribution for the case of $\mu \approx 0$ [56].

Due to the complexity of tight-binding calculations (notice that the cylindrical symmetry and angular-momentum conservation no longer apply, and scattering cannot be described independently for each normal mode, as in previous sections; instead, the mode mixing occurs [47]) the physical size of the system is reduced. Namely, we took $W_\infty = 700 a_0$ (the lead width) and the radii $r_1 = 50 a_0$, $r_2 = 200 a_0$. In effect, the energy separating weak- and the high-doping regimes is $\hbar v_F / r_1 = 46.8$ meV, the number of sites in the sample area equals 136,035 (comparing to the total no. of 336,000

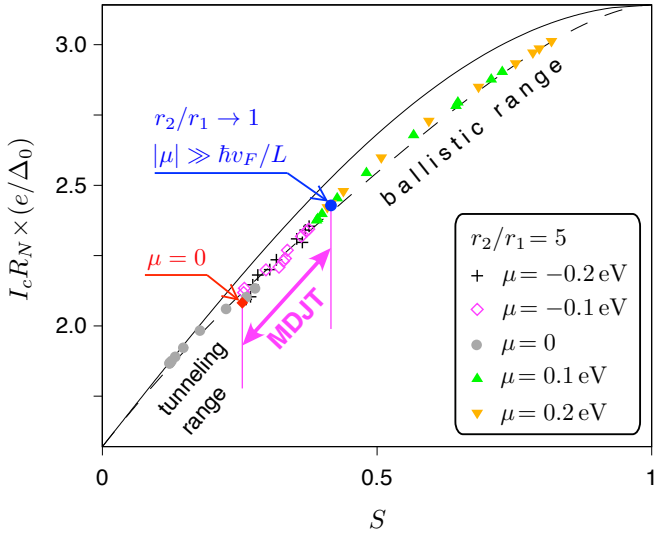


Figure 6: Product $I_c R_N$ displayed versus the skewness for smooth potentials (datapoints). Each dataset contains ten datapoints corresponding to $m = 2, 4, \dots, 512$, and $m = \infty$, for one of five fixed values of the chemical potential, $\mu = -0.2, -0.1, \dots, 0.2$ eV (see the legend). Remaining system parameters are same as in Fig. 4. Two additional symbols (full circle and diamond) mark the values given in Eqs. (22) and (31), separating the crossovers to SJT (lower values), the MDJT regime (middle), and the crossover to BJE (higher values). Solid/dashed black lines are same as in Fig. 3.

sites placed between the semi-infinite leads at a distance of $120\sqrt{3}a_0 \simeq 51.1$ nm). The details of the computational technique can be found in Ref. [47]. Similarly as before, the eigenvalues (T_n) of the matrix tt^\dagger , where the transmission matrix $t = (t_{mn})$, $m = 1, \dots, N_R$, $n = 1, \dots, N_L$, and N_R (N_L) denotes the number of modes in the right (left) lead, are determined for a given Fermi energy E , the normal-state conductance as well as the Josephson current can be evaluated via Eqs. (5) and (6).

B. Relation to the continuous model

It is a notable feature of the half-disk geometry that considerations for the continuous model (i.e., starting from the Dirac equation) [12, 40], with the mass confinement [57] and $V_0, m \rightarrow \infty$ in Eq. (2), lead to identical transmission eigenvalues (T_j) as given by Eq. (17), with the $\mu \rightarrow 0$ limits $T_j(0)$ given by Eq. (19), but the quantum number j takes the positive values, $j = \frac{1}{2}, \frac{3}{2}, \dots$. In effect, the pseudodiffusive values of $I(\theta)$ and R_N^{-1} given by Eqs. (20) and (21), need to be divided by a factor of 2; the same applies for the sub-Sharvin results given by Eqs. (29) and (30). In particular, for $|\mu| \gg \hbar v_F/r_1$ and $r_2 \gg r_1$, we get

$$R_N^{-1} \simeq (4 - \pi) G_{\text{Sharvin}}, \quad (40)$$

with $G_{\text{Sharvin}} = g_0 r_1 |\mu| / (\hbar v_F)$ this time.

We further notice that intensive quantities, such as the product $I_c R_N$ and the skewness S are unaffected upon the disk

halving, as long as the Dirac-equation limit is considered. For the Dirac point $|\mu| \ll \hbar v_F/r_1$ and a finite $r_2/r_1 = 4$, substituting $T_j(0)$ -s given by Eq. (19) into Eqs. (5), (6), and summing over $j = \frac{1}{2}, \frac{3}{2}, \dots$ leads to

$$I_c R_N \frac{e}{\Delta_0} = 1.92571, \quad S = 0.149323. \quad (41)$$

Similarly as for $r_2/r_1 = 5$ (see Table I), the above values are significantly lower than their pseudodiffusive counterparts given in Eq. (22).

C. Numerical results

The results for our tight-binding simulations are presented in Fig. 7. Since the evolution with the exponent m , see Eq. (2), is systematic, we limit the presentation in (a)–(c) to the parabolic ($m = 2$) and rectangular ($m = \infty$) profiles. In particular, the conductance spectrum in (a) is approximately symmetric (upon $\mu \leftrightarrow -\mu$) for $m = \infty$ if $|\mu|/t_0 \lesssim 0.2$. For $\mu/t_0 \lesssim -0.2$, the number of propagating modes in the left (narrow) lead, $N_L \simeq r_1 |V_0 + \mu| / (\hbar v_F) \lesssim 17$, and the conductance reduction becomes significant. Additionally, for $\mu/t_0 \gtrsim -0.2$, numerical results are close to the sub-Sharvin values given by $(4 - \pi) G_{\text{Sharvin}}$ [dashed line].

Also in Fig. 7(a) but for $m = 2$, we identify strong conductance suppression for the tripolar doping ($\mu < 0$), where the resonances with quasi-bound states, earlier observed for the continuous model (see Fig. 4), are virtually absent. This can be attributed partly to the lattice discretization, and partly to the group velocity mismatch due to trigonal warping. In contrast, for the unipolar doping ($\mu > 0$), the reduction is only moderate in comparison to the expected ballistic value [40]

$$G_{\text{Sharvin}}^{(2)} \approx (r_c/r_1) G_{\text{Sharvin}}^{(\infty)}, \quad (42)$$

with $G_{\text{Sharvin}}^{(\infty)} \equiv G_{\text{Sharvin}}$, shown with black solid line. The effect is less apparent for longer Fermi wavelengths (see the inset), suggesting that the behavior of the continuous model will presumably be restored for a sufficiently large lattice system.

Remarkably, for the product $I_c R_N$, see Figs. 7(b,c), is rather weakly affected by the above-mentioned lattice-related factors. For $m = \infty$, most of the data — in the whole range of $|\mu|/t_0 \leq 0.2$ considered — lay within the MDJT range (yellow area) defined by the values given in Eqs. (22) and (31), with the exception of a small vicinity of $\mu = 0$, where the value given in Eq. (41) is closely approached. For $m = 2$, the oscillations of Fabry-Pérot type are well pronounced, particularly for $\mu < 0$ where both R_N^{-1} and I_c are strongly suppressed, but most of the data lie below the lower bound given by Eq. (22) for the pseudodiffusive limit, showing that the suppression of I_c is stronger than for R_N^{-1} . This observation coincides with another one for $m = 2$ and $\mu > 0$, where the product $I_c R_N$ does not exceed the upper bound given in Eq. (31) for the sub-Sharvin limit. Both findings show that the reduction of I_c in the tight-binding simulation, when compared

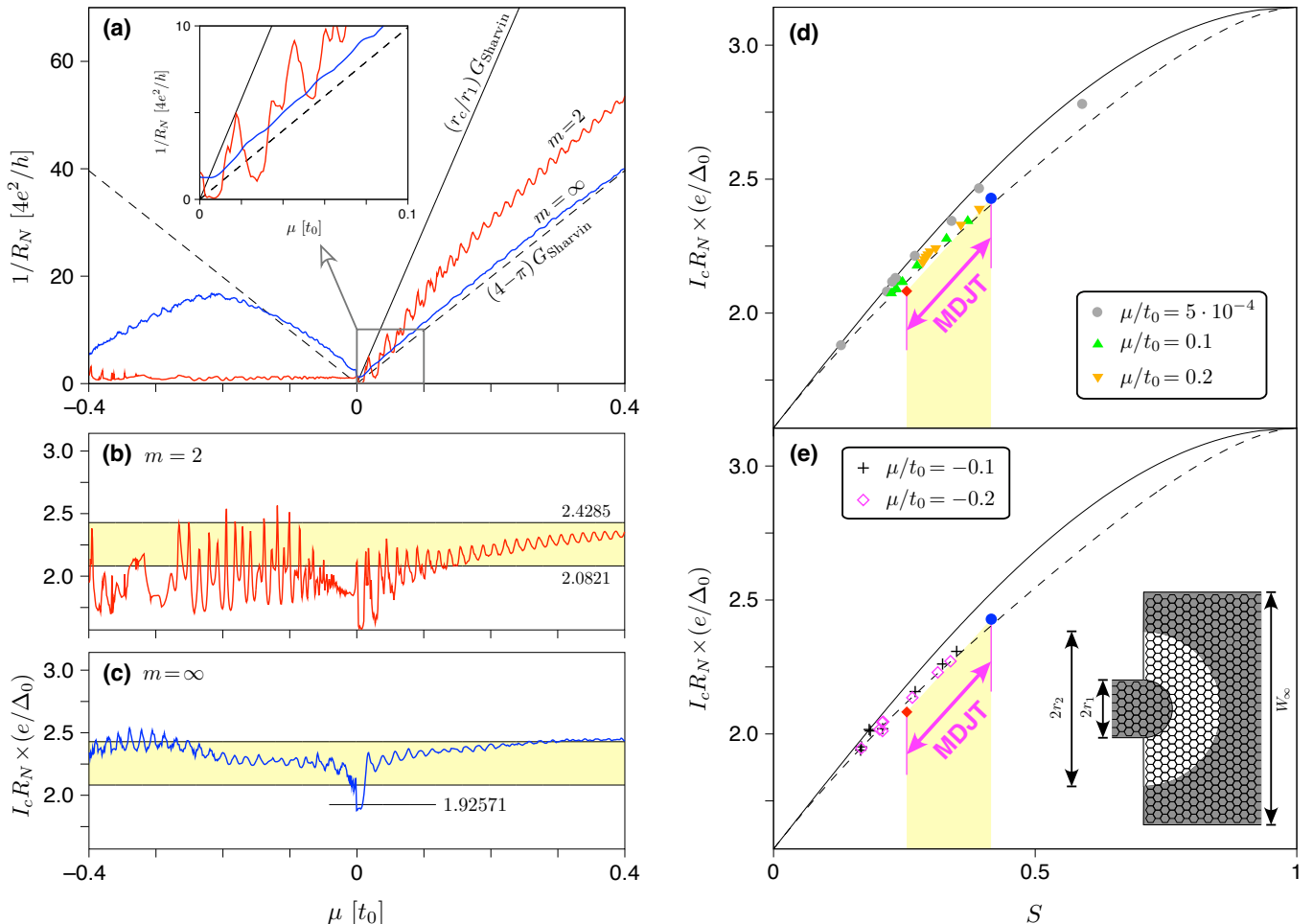


Figure 7: (a)–(e) Normal-state conductance $1/R_N$ in the units of $g_0 = 4e^2/h$ (a), the product $I_c R_N$ in the units of Δ_0/e (b,c) as functions of the chemical potential (specified in the units of $t_0 = 2.7 \text{ eV}$) and the critical current—skewness diagram (d,e) for the half-Corbindo disk, shown schematically in (e). The system parameters are $W_\infty = 700 a_0$, $r_2 = 4r_1 = 200 a_0$. (a–c) Color thick lines represent the numerical results the potential profiles given by Eq. (2) with $m = 2$ [red] and $m = \infty$ [blue]. Black thin lines in (a) depict the ballistic approximation for a continuous system, $(r_c/r_1) G_{\text{Sharvin}}$ with $G_{\text{Sharvin}} = g_0 r_1 |\mu| / (\hbar v_F)$ [solid] and the sub-Sharvin conductance $(4 - \pi) G_{\text{Sharvin}}$ [dashed]. (Inset is a zoom-in, for $0 \leq \mu/t_0 \leq 0.1$, of the data shown in the main panel.) Horizontal lines bounding the yellow areas (b,c) are same as in Fig. 5. Additional horizontal line in (c) marks the value of $I_c R_N$ for $r_2/r_1 = 4$ and $V_0, m \rightarrow \infty$ in the continuous model, see Eq. (41). (d,e) Each dataset contains eight datapoints corresponding to $m = 2, 4, \dots, 128$, and $m = \infty$, for one of fixed values of the chemical potential, i.e., $\mu/t_0 = 5 \cdot 10^{-4}$, 0.1, 0.2 (d), or $\mu/t_0 = -0.1$, $\mu/t_0 = -0.2$ (e) [see the legend]. Solid/dashed black lines are same as in Fig. 3; two additional symbols (full circle and diamond) bounding the MDJT range are same as in Fig. 6.

to the continuous model, which clearly demonstrates the sub-Sharvin-to-ballistic crossover for $\mu > 0$ (see Fig. 5), is more significant than for the case of R_N^{-1} illustrated in Fig. 7(a).

Finally, in Figs. 7(d,e), we present the critical current — skewness diagrams for the tight-binding results obtained for all values of $m = 2, 4, \dots, 128$ and $m = \infty$ considered in our study. The values of μ/t_0 are fixed at $5 \cdot 10^{-4}$ (for technical reasons, we took a small nonzero value), 0.1 and 0.2 in (d), or $\mu/t_0 = -0, 1, -0.2$ in (e).

In contrast to the analogous diagram for the continuous model, see Fig. 6, the datapoints for $\mu \approx 0$ [grey circles] are now spread over a much wider range, showing the tunneling-to-ballistic crossover, and closely follow the single-mode approximation [solid lines]. This can be attributed to the presence of edge states propagating along the free boundaries of

the sample [56]. The propagation through such states, albeit suppressed for flat potential profiles ($m \rightarrow \infty$) due to the potential variation on edge atoms, reappears for smaller m -s, as the weakly-doped area gets shrunk to the narrow neighborhood of $r \approx r_c$.

The datapoints for $\mu > 0$, as well as for $\mu < 0$, follow the multimode toy model, see Eqs. (37) and (38) [dashed lines]. For $\mu > 0$, the results stay within (or are very close to) the borders of MDJT range, although previously (i.e., for the continuous model) the sub-Sharvin-to-ballistic crossover was observed. For $\mu < 0$, the datasets are shifted such that they partly cover the MDJT range, also taking the values below the lower bounds for $I_c R_N$ and S .

It can be seen from Figs. 7(d,e) that — except from the vicinity of $\mu = 0$ — a generic reduction of transmission prob-

abilities in the tight-binding model (if compared to the continuous model) leads to smaller values of both $I_c R_N$ and S , shifting the system characteristic towards the tunneling regime.

VI. CONCLUDING REMARKS

We have investigated the characteristics of the Corbino-Josephson setup in graphene, including the normal-state conductance, critical current, and the skewness of the current phase relation, supposing that the radial profile of electrostatic potential barrier is tuned from a parabolic to a rectangular shape. The detailed interpretation of the barrier smoothing is left out of the scope of this work; in principle, it can be regarded as an intrinsic feature of the device, grasped within a self-consistent solution including the carrier diffusion and manifesting itself primarily by the asymmetry of the conductance spectrum [15, 20, 42], but one can also expect — in particular, for ultraclean graphene-on-hBN devices [18] — that additional gate electrodes may allow one to tune the barrier electrostatically (at least to some degree).

Our results show that the system behavior possible for the rectangular barrier of an infinite height, earlier discussed in Ref. [30], is substantially enriched when smooth potentials are under consideration. Namely, the product product of critical current and normal-state resistance ($I_c R_N$) and skewness of the current-phase relation (S) analyzed within the continuous model utilizing the Dirac-Bogoliubov-De-Gennes equation exhibit — when tuning the barrier profile — crossovers between three types of behavior possible for a generic Josephson junction. A standard Josephson tunneling (SJT), with the supercurrent governed by a single mode, is approached near the charge-neutrality point for the values of the disk radii ratio starting from $r_2/r_1 = 4 \div 5$ and flat (i.e., nearly-rectangular) barriers, graphene-specific multimode Dirac-Josephson tunneling (MDJT) occurs for the tripolar doping and wide collection of barrier shapes, or for unipolar doping and flat barriers, the ballistic Josephson effect (BJE) is reconstructed for unipolar doping and smooth (nearly parabolic) barriers.

The picture following from the continuous model, and for the mesoscopic device of approx. $0.5 \mu\text{m}$ in diameter, is confronted with the tight-binding simulation of a smaller, approx. 100 nm in diameter, half-disk device. The relevant transport characteristics, for both the normal and superconducting contacts, are suppressed due to finite-size (and lattice-specific) factors, and the suppression is noticeably stronger for superconducting contacts resulting in reduced values of the product $I_c R_N$ and S for nearly all physical regimes; however, for the suppression is marginal for SJT and MDJT regimes for flat (or nearly flat) barriers. These findings support the key observations for the continuous model, suggesting that if the system size is within the mesoscopic range, the factors such as lattice discretization and trigonal warping of the dispersion relation would not significantly affect the measurable quantities.

The Corbino-Josephson device in graphene, here discussed assuming the short-junction limit and in the absence of magnetic field, are put forward as a versatile system allowing not only for electrostatic control over the critical current, but also for electrostatic switching between different classes of Josephson effects in the mesoscopic limit. We hope this study would stimulate follow-up discussions, possibly addressing the problem of macroscopic quantum effects [58, 59] and quantum information [60] as the (controlled) crossover between single- and multiple-mode Josephson effects may also allow for temperature-independent control over the quantum coherence.

Acknowledgments

The work was partly completed during a sabbatical granted by the Jagiellonian University in the summer semester of 2024/25. We gratefully acknowledge Polish supercomputing infrastructure PLGrid (HPC Center: ACK Cyfronet AGH) for providing computer facilities and support within computational grants Nos. PLG/2025/018544 (partly) and PLG/2025/018379.

-
- [1] L. Boltzmann, On some experiments relating to Hall's phenomenon, *Phil. Mag.* **22**, 226 (1886).
 - [2] O. M. Corbino, Azioni Elettromagnetiche Doyute Agli Ioni dei Metalli Deviate Dalla Traietoria Normale per Effetto di un Campo, *Nuovo Cim.* **1**, 397 (1911).
 - [3] E. P. Adams, The Hall and Corbino effects, *Proc. Am. Phil. Soc.* **54**, 47 (1915).
 - [4] For a comprehensive review of early-stage researches, see: S. Galdamini and G. Giuliani, Magnetic field effects and dualistic theory of metallic conduction in Italy (1911–1926): cultural heritage, creativity, epistemological beliefs, and national scientific community, *Ann. Sci.* **48**, 21 (1991).
 - [5] G. Kirczenow, Quantum transport in ballistic nano-scale Corbino disks, *J. Phys.: Condens. Matter* **6**, L583 (1994).
 - [6] S. Souma and A. Suzuki, Effect of impurity scattering in nanoscale Corbino disks, *Phys. Rev. B* **58**, 4649 (1998).
 - [7] R. G. Mani, Steady-state bulk current at high magnetic fields in Corbino-type GaAs/AlGaAs heterostructure devices, *Europhys. Lett.* **36**, 203 (1996).
 - [8] N. d'Ambrumenil and R. H. Morf, Thermopower in the quantum Hall regime, *Phys. Rev. Lett.* **111**, 136805 (2013).
 - [9] S. F. W. R. Rycroft, R. A. Doyle, D. T. Fuchs, E. Zeldov, R. J. Drost, P. H. Kes, T. Tamegai, S. Ooi, and D. T. Foord, Bulk transport properties of $\text{Bi}_2\text{Sr}_2\text{CaCu}_2\text{O}_8$ crystals in the Corbino disk geometry, *Phys. Rev. B* **60**, 757(R) (1999).
 - [10] See, e.g.: M. I. Katsnelson, *The Physics of Graphene. Second Edition*, (Cambridge University Press, Cambridge, UK, 2020). DOI: <https://doi.org/10.1017/9781108617567>, Chapter 3.
 - [11] V. V. Cheianov and V. I. Fal'ko, Selective transmission of Dirac electrons and ballistic magnetoresistance of n-p junctions in graphene, *Phys. Rev. B* **74**, 041403(R) (2006).
 - [12] A. Rycerz, P. Recher, and M. Wimmer, Conformal mapping and shot noise in graphene, *Phys. Rev. B* **80**, 125417 (2009).

- [13] A. Rycerz, Magnetoconductance of the Corbino disk in graphene, *Phys. Rev. B* **81**, 121404(R) (2010).
- [14] Z. Khatibi, H. Rostami, and R. Asgari, Valley polarized transport in a strained graphene based Corbino disc, *Phys. Rev. B* **88**, 195426 (2013).
- [15] E. C. Peters, A. J. M. Giesbers, M. Burghard, and K. Kern, Scaling in the quantum Hall regime of graphene Corbino devices, *Appl. Phys. Lett.* **104**, 203109 (2014).
- [16] B. Abdollahipour and E. Moomivand, Magnetopumping current in graphene Corbino pump, *Physica E* **86** 204 (2017).
- [17] A. Rycerz, Wiedemann–Franz law for massless Dirac fermions with implications for graphene, *Materials* **14**, 2704 (2021).
- [18] Y. Zeng, J. I. A. Li, S. A. Dietrich, O. M. Ghosh, K. Watanabe, T. Taniguchi, J. Hone, and C. R. Dean, High-Quality Magnetotransport in Graphene Using the Edge-Free Corbino Geometry, *Phys. Rev. Lett.* **122**, 137701 (2019).
- [19] D. Suszalski, G. Rut, and A. Rycerz, Mesoscopic valley filter in graphene Corbino disk containing a p-n junction, *J. Phys. Mater.* **3**, 015006 (2020).
- [20] M. Kamada, V. Gall, J. Sarkar, M. Kumar, A. Laitinen, I. Gornyi, and P. Hakonen, Strong magnetoresistance in a graphene Corbino disk at low magnetic fields, *Phys. Rev. B* **104**, 115432 (2021).
- [21] Y. Yerin, V. P. Gusynin, S. G. Sharapov, and A. A. Varlamov, Genesis and fading away of persistent currents in a Corbino disk geometry, *Phys. Rev. B* **104**, 075415 (2021).
- [22] M. Titov and C. W. J. Beenakker, Josephson effect in ballistic graphene, *Phys. Rev. B* **74**, 041401(R) (2006).
- [23] A. G. Moghaddam and M. Zareyan, Josephson effect in mesoscopic graphene strips with finite width, *Phys. Rev. B* **74**, 241403(R) (2006).
- [24] I. Hagymási, A. Kormányos, and J. Cserti, Josephson current in ballistic superconductor-graphene systems, *Phys. Rev. B* **82**, 134516 (2010).
- [25] M. Alidoust and J. Linder, Tunable supercurrent at the charge neutrality point via strained graphene junctions, *Phys. Rev. B* **84**, 035407 (2011).
- [26] V. E. Calado, S. Goswami, G. Nanda, M. Diez, A. R. Akhmerov, K. Watanabe, T. Taniguchi, T. M. Klapwijk, and L. M. K. Vandersypen, Ballistic Josephson junctions in edge-contacted graphene, *Nature Nanotech.* **10**, 761 (2015).
- [27] C. D. English, D. R. Hamilton, C. Chialvo, I. C. Moraru, N. Mason, and D. J. Van Harlingen, Observation of nonsinusoidal current-phase relation in graphene Josephson junctions, *Phys. Rev. B* **94**, 115435 (2016).
- [28] G. Nanda, J. L. Aguilera-Servin, P. Rakyta, A. Kormányos, R. Kleiner, D. Koelle, K. Watanabe, T. Taniguchi, L. M. K. Vandersypen, S. Goswami, Current-Phase Relation of Ballistic Graphene Josephson Junctions, *Nano Lett.* **17**, 3396 (2017).
- [29] R. J. Wojciechowski, and L. Kowalewski, Josephson Effect in Graphene-Based Junctions, *Acta Phys. Pol. A* **133**, 632 (2018).
- [30] B. Abdollahipour, R. Mohammadkhani, and M. Khalilzadeh, Josephson current in ballistic graphene Corbino disk, *Superlatt. Microstruct.* **118**, 177 (2018).
- [31] K.-F. Huang, Y. Ronen, R. Mélin, D. Feinberg, K. Watanabe, T. Taniguchi, and P. Kim, Evidence for $4e$ charge of Cooper quartets in a biased multi-terminal graphene-based Josephson junction, *Nat. Commun.* **13**, 3032 (2022).
- [32] F. Zhang, A. S. Rashid, M. T. Ahari, W. Zhang, K. M. Anantharayanan, R. Xiao, G. J. de Coster, M. J. Gilbert, N. Samarth, and M. Kayyalha, Andreev processes in mesoscopic multi-terminal graphene Josephson junctions, *Phys. Rev. B* **107**, L140503 (2023).
- [33] P. S. Banerjee, R. Marathe, and S. Ghosh, Magnetically modulated Superconductor-Graphene-Superconductor (SGS) Josephson junctions and their tunability, *Phys. Scr.* **100**, 015965 (2024).
- [34] S. Jang, G.-H. Park, K. Watanabe, T. Taniguchi, and G.-H. Lee, Edge dependence of the supercurrent in the quantum Hall regime,
- [35] A. Rycerz, Sub-Sharvin conductance and Josephson effect in graphene, e-print: arXiv:2603.01269 (unpublished).
- [36] R. Cristiano, M. P. Lisitskii, C. Nappi, and A. Barone, Fiske resonances in annular Josephson junctions, *Phys. Rev. B* **62**, 8683 (2000).
- [37] R. H. Hadfield, G. Burnell, D.-J. Kang, C. Bell, and M. G. Blamire, Corbino geometry Josephson junction, *Phys. Rev. B* **67**, 144513 (2003).
- [38] Y. Zhang, Z. Lyu, X. Wang, E. Zhuo, X. Sun, B. Li, J. Shen, G. Liu, F. Qu, and L. Lü, Ac Josephson effect in Corbino-geometry Josephson junctions constructed on Bi_2Te_3 surface, *Chinese Phys. B* **31**, 107402 (2022).
- [39] A. Rycerz and P. Witkowski, Sub-Sharvin conductance and enhanced shot noise in doped graphene, *Phys. Rev. B* **104**, 165413 (2021).
- [40] A. Rycerz and P. Witkowski, Theory of the sub-Sharvin charge transport in graphene disks, *Phys. Rev. B* **106**, 155428 (2022).
- [41] A. Tomadin, G. Vignale, and M. Polini, Corbino Disk Viscometer for 2D Quantum Electron Liquids, *Phys. Rev. Lett.* **113**, 235901 (2014).
- [42] C. Kumar, J. Birkbeck, J. A. Sulpizio, D. Perello, T. Taniguchi, K. Watanabe, O. Reuven, T. Scaffidi, A. Stern, A. K. Geim, and S. Ilani, Imaging hydrodynamic electrons flowing without Landauer–Sharvin resistance, *Nature* **609**, 276 (2022).
- [43] A. Levchenko, S. Li, and A. V. Andreev, Hydrodynamic magnetoresistance in graphene Corbino devices, *Phys. Rev. B* **106**, L201306 (2022).
- [44] S. Vijayakrishnan, Z. Berkson-Korenberg, J. Mainville, L. W. Engel, M. P. Lilly, K. W. West, L. N. Pfeiffer, and G. Gervais, Two-dimensional hydrodynamic viscous electron flow in annular Corbino rings, *Phys. Rev. Research* **7**, L022029 (2025).
- [45] J. Tworzycyło, B. Trauzettel, M. Titov, A. Rycerz, and C. W. J. Beenakker, Sub-Poissonian shot noise in graphene, *Phys. Rev. Lett.* **96**, 246802 (2006).
- [46] F. Miao, S. Wijeratne, Y. Zhang, U. C. Coskun, W. Bao, C. N. Lau, Phase Coherent Transport in Graphene Quantum Billiards, *Science* **317**, 1530 (2007).
- [47] A. Rycerz, The Quantum Transport of Dirac Fermions in Selected Graphene Nanosystems Away from the Charge Neutrality Point, *Materials* **18**, 2036 (2025).
- [48] A. Laitinen, G. S. Paraoanu, M. Oksanen, M. F. Craciun, S. Russo, E. Sonin, and P. Hakonen, Contact doping, Klein tunneling, and asymmetry of shot noise in suspended graphene, *Phys. Rev. B* **93**, 115413 (2016).
- [49] G. S. Paraoanu, Klein tunneling through the trapezoidal potential barrier in graphene: conductance and shot noise, *New J. Phys.* **23**, 043027 (2021).
- [50] C. W. J. Beenakker, Specular Andreev Reflection in Graphene, *Phys. Rev. Lett.* **97**, 067007 (2006).
- [51] C. W. J. Beenakker, Three "universal" mesoscopic Josephson effects, in *Transport Phenomena in Mesoscopic Systems*, edited by H. Fukuyama and T. Ando (Springer, Berlin, 1992). doi:10.1007/978-3-642-84818-6_22.
- [52] M. Büttiker, Y. Imry, R. Landauer, and S. Pinhas, Generalized many-channel conductance formula with application to small rings, *Phys. Rev. B* **31**, 6207 (1985).
- [53] An important step in the derivation of Eq. (17) is the recognition of the Wronskian of Hankel functions, see M. Abramowitz

- and I. A. Stegun, eds., *Handbook of Mathematical Functions* (Dover Publications, Inc., New York, 1965), Chapter 9, Eq. 9.1.17.
- [54] S. Datta, *Electronic Transport in Mesoscopic Systems* (Cambridge University Press, Cambridge, UK, 1997), Chapter 3, p. 129.
- [55] K. J. U. Vidarte and C. Lewenkopf, High-energy Landau levels in graphene beyond nearest-neighbor hopping processes: Corrections to the effective Dirac Hamiltonian, *Phys. Rev. B* **106**, 155414 (2022).
- [56] M. Wimmer, Quantum transport in nanostructures: From computational concepts to spintronics in graphene and magnetic tunnel junctions, PhD Thesis (Universität Regensburg, Regensburg, Germany, 2009). <https://epub.uni-regensburg.de/12142/1/wimmer.pdf>.
- [57] M. V. Berry and R. J. Mondragon, Neutrino billiards: time-reversal symmetry-breaking without magnetic fields, *Proc. R. Soc. Lond. A* **412**, 53 (1987).
- [58] J. M. Martinis, M. H. Devoret, and J. Clarke, Energy-Level Quantization in the Zero-Voltage State of a Current-Biased Josephson Junction, *Phys. Rev. Lett.* **55**, 1543 (1985).
- [59] M. H. Devoret, J. M. Martinis, and J. Clarke, Measurements of Macroscopic Quantum Tunneling out of the Zero-Voltage State of a Current-Biased Josephson Junction, *Phys. Rev. Lett.* **55**, 1908 (1985).
- [60] G. Wendin, Quantum information processing with superconducting circuits: a review, *Rep. Prog. Phys.* **80** 106001 (2017).